Ultrasonics 101 (2020) 106003

Contents lists available at ScienceDirect

Ultrasonics

journal homepage: www.elsevier.com/locate/ultras

Acoustic analysis of ultrasonic assisted soldering for enhanced adhesion

Ken F. Maassen[a,b], Jennifer Shaffer Brown[b], Hongseok Choi[b], Lonny L. Thompson[b], Joshua B. Bostwick[b,*]

[a] George W. Woodruff School of Mechanical Engineering, Georgia Institute of Technology, Atlanta, GA 30332, USA
[b] Department of Mechanical Engineering, Clemson University, Clemson, SC 29634, USA

ABSTRACT

Ultrasonic soldering utilizes high-intensity acoustic fields to induce cavitation in the solder melt in order to (i) bond dissimilar materials and (ii) improve solder joint strength. The acoustic energy transfer from the piezoelectric transducer (PZT) into the liquid solder pool is critical in both understanding and optimizing this process. We use finite element analysis of the acoustics and compare with experiment. Our finite-element modeling approach is two-pronged; (i) we develop a one-dimensional model that is used as a design tool to optimize the solder stack geometry to match the transducer frequency for maximal acoustic energy transfer and (ii) we use a three-dimensional model to compute the frequency response in the solder stack assembly (solid acoustics) and the acoustic pressure in the liquid solder pool (solid-fluid interaction). The acoustic pressure is a proxy for cavitation and therefore bond strength. Our simulations show the acoustic pressure rapidly decreases as the height of the solder tip above the substrate surface increases, which correlates with controlled experiments that show the solder bond quality also decreases with increasing tip height.

1. Introduction

Soldering sees widespread use in industrial applications such as the assembly of circuit boards, where typically tin-based solder is used to bond electrical components to copper circuit boards. Ultrasonic soldering has been long studied as an alternative to conventional soldering, because it (i) eliminates the use of environmentally-harmful flux and (ii) allows for the use of low-melt temperature lead-free solder to achieve similar joint quality [1–5]. Most importantly, ultrasonic soldering allows for the bonding of dissimilar substrates, such as metal to glass (ceramic) [6–8]. Flux is used in conventional soldering to scrub away the oxide layer on a metallic substrate, as oxides typically reduce wetting and adhesion thereby degrading joint quality [9]. In addition, flux often increases the electrical resistivity in the joint and has a negative environmental impact. Ultrasonic soldering uses high-intensity acoustic fields to induce cavitation or bubble formation in the liquid solder pool, as shown in Fig. 1(*a*). When these bubbles collapse they generate large localized pressures and temperatures that remove the oxide layer from the substrate and allow a good adhesive bond between dissimilar materials. This is sometimes referred to as erosion [10,11]. In this paper, we are interested in modeling and optimizing the acoustic energy transfer from the PZT ultrasonic transducer through the soldering iron assembly and into the molten solder pool to both understand and improve the ultrasonic soldering process.

The ultrasonic soldering process is a complex multi-physics problem that involves fluid mechanics, heat transfer, phase change, solidification, wetting and adhesion [3]. Our research team has recently developed an automated ultrasonic soldering platform, adapted from a commercially available 3D printer, that allows for precise control of the process parameters (cf. Fig. 1). For a fixed set of experimental conditions, Fig. 1(*b*) illustrates the difference between solder lines with (left) and without (right) ultrasonics. Note that both lines are made from identical solder volumes, but the solder line with ultrasonics wets the glass substrate much better. Furthermore, inspection of the solder/substrate interface reveals the presence of a large number of voids in the non-ultrasonicated sample. This can be seen with the naked eye in Fig. 1(*b*) as a hazy finish, whereas the ultrasonicated sample has a mirror finish indicative of the relative absence of voids. Here voids are simply bubbles that have been 'frozen' into the solder joint during the solidification process. The presence of voids degrades the mechanical solder/substrate bond, as it decreases bond contact; optimal adhesion corresponds to 100% contact area. Our preliminary experiments show the joint quality (proxy for number of voids) depends strongly upon the (i) strength of the acoustic field and (ii) location of the solder tip above the glass substrate.

There is a vast literature on bubble dynamics and collapse, most of which builds upon the famous Rayleigh-Plesset equation describing the dynamics of a spherical bubble in an infinite medium [12,13]. Here the acoustic field appears as a far-field pressure that drives bubble motion [14]. For modern reviews of bubble dynamics and cavitation and applications thereof, see [15–18]. The presence of a solid boundary complicates the bubble dynamics. In ultrasonic soldering, the bubbles

* Corresponding author.
E-mail address: jbostwi@clemson.edu (J.B. Bostwick).

https://doi.org/10.1016/j.ultras.2019.106003
Received 25 May 2019; Received in revised form 20 August 2019; Accepted 2 September 2019
Available online 09 September 2019

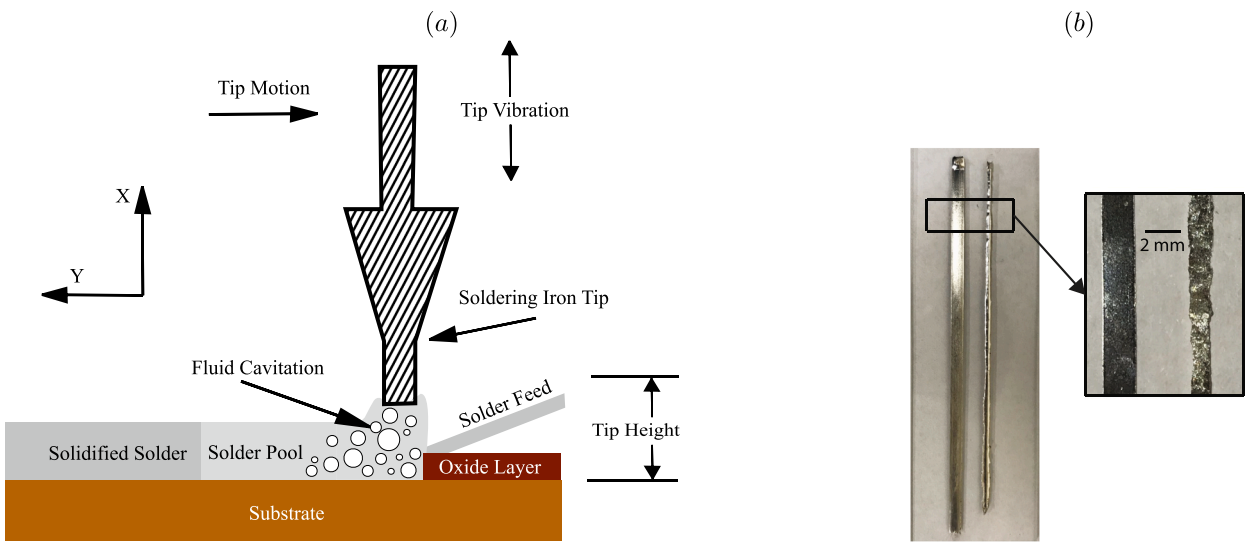

Fig. 1. Schematic of the ultrasonic assisted soldering process. (a) Solder is fed into a heated tip that moves at a height h above a glass substrate resulting in a molten solder pool. Ultrasonic energy is transmitted to the solder melt through tip vibration from the ultrasonic transducer causes the rapid formation and collapse (cavitation) of bubbles in the solder melt that leads to improved wetting and adhesion. (*b*) Two solder lines with identical volume of solder illustrate the difference in wetting behavior with ultrasonics (left) and without ultrasonics (right). The inset to sub-figure (*b*) shows the underside of the glass substrate to illustrate the difference in void formation at the solder/substrate interface.

near the substrate are critically important and subject to phenomena like primary and secondary Bjerknes forces that cause net translation [19]. For cavitation bubbles near a solid boundary, such as the substrate surface, a local pressure gradient is formed on the bubble surface where the pressure near the solid surface becomes significantly lower than the opposite side. This pressure gradient leads to asymmetric bubble collapse whereby a reentrant liquid jet penetrates into the collapsing bubble and impinges on the solid surface [20]. The impinging liquid jet provides additional energy to help clean the solid surface and improve adhesion. It is hypothesized that this 'cleaning process' removes the oxide layer and allows the solder to better adhere to the substrate [21]. With regard to our ultrasonic soldering application, it is critical to know the details of how the acoustic field propagates through the solid and into the solder melt in order to better understand the mechanism for enhanced adhesion. This is our focus.

Acoustic energy in our system is generated by passing an electrical signal into the transducer, consisting of a piezoelectric material (PZT) sandwiched between two masses, which generates a mechanical response producing an acoustic wave that travels through the assembly to the tool tip and into the solder pool, where the compression and rarefaction waves work to grow and then cavitate microscopic bubbles in the fluid [22]. After bubble expansion during the rarefaction phase of ultrasound, the bubble freely collapses resulting in a shock wave emission [23]. This study focuses on modeling acoustic energy transfer from the transducer through the soldering iron tip (solid) and into the molten solder pool (fluid). A detailed three-dimensional (3D) finite element analysis of two different soldering iron assemblies is used to demonstrate the need for tuning the resonance frequency of the stack assembly to match the operating frequency of the control unit in order to maximize the ultrasonic energy delivered to the molten solder pool.

A commercially available hand-held Ultrasonic Assisted Soldering (UAS) system (hereafter called Type A) is shown in Fig. 2 with materials and mechanical boundary conditions labeled. The length of the center section has been redacted for proprietary reasons. Our automated system uses a different assembly, which we will refer to as Type B, with different cross-section dimensions and segment lengths; details are not shown for propriety reasons. Finite element analysis is used to understand the acoustics (i) in the solder iron assembly (solid) and (ii) from the solder tip to the molten solder pool.

For the purposes of this paper, the performance of the UAS system is based on the ability to increase adhesion. Current theories propose that increased adhesion from UAS results from cavitation generated by the oscillating acoustic pressure wave [24]. Since the frequency is imposed by the ultrasonic power supply, the pressure amplitude in the liquid solder melt can be considered the response variable, and the soldering iron geometry and material parameters are the design variables. For efficient power transfer, the tip displacement during vibration should be maximized to deliver the greatest pressure in the solder melt. To that end, a simplified one-dimensional finite element model of the solder iron assembly is developed and used as a design tool to quickly modify the geometry for optimal tuning to the transducer. We validate the 1D model by comparing the frequency response of the solder iron assemblies to the detailed 3D model. Lastly, a coupled solid-fluid finite element model is created and used to analyze the effect of varying tip height on acoustic pressure in the molten solder pool which we correlate with solder bond quality in experiment.

2. Solid acoustics

The Type A soldering iron assembly consists of the stainless steel solder tip, piezoelectric transducer, and aluminum end caps shown in Fig. 2. The Type B assembly has a similar construction but is redacted for proprietary reasons. Material properties for the 316 stainless steel, aluminum, and PZT (Lead Zirconate Titanate) are given in Table 1. The properties of stainless steel and aluminum materials were taken from the default engineering data in ANSYS, while those for the PZT material were obtained from [25], with Poisson's ratio derived from the mechanical compliance relationships. The commercial finite element software ANSYS is used to analyze the solid acoustics of the solder iron assemblies. Boundary conditions are applied at the locations shown in Fig. 2. We fix the displacements around the perimeter of the thin support ring to replicate the attachment of the soldering iron to its holder. By design, the support ring is a thin circular annulus designed to offer little axial stiffness along the solder iron length (in this case the resonance frequencies for axial modes correspond to free-free conditions). The ANSYS finite element solver is used to analyze the frequency response.

Assuming time-harmonic loading and response with $e^{-i\omega t}$, where $i = \sqrt{-1}$, and ω is the circular frequency in rad/s, the assembled finite element equations for the soldering iron take the matrix form,

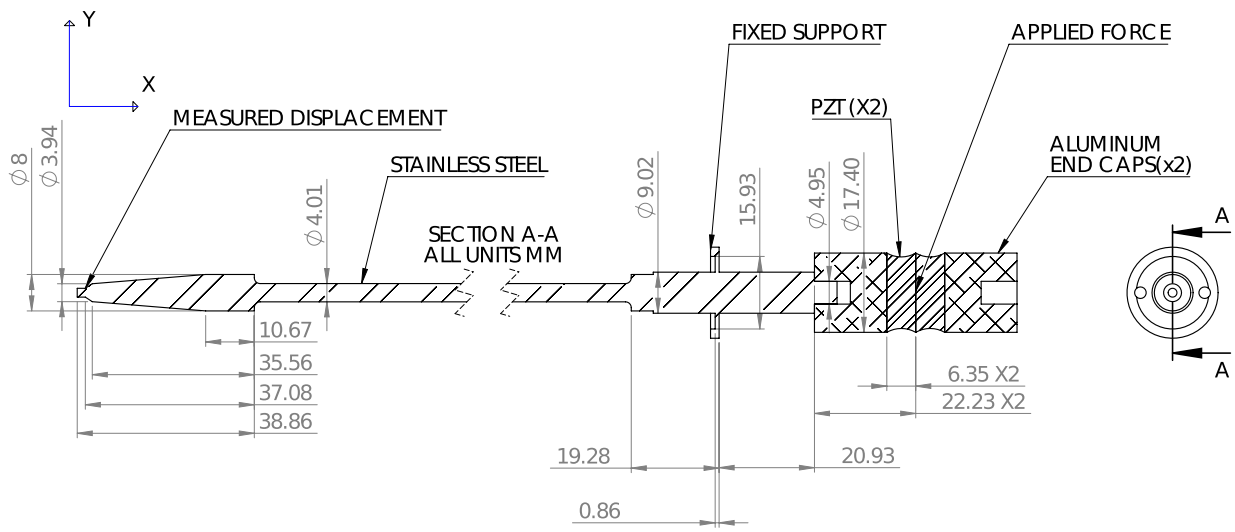

Fig. 2. Drawing of the Type A UAS iron and transducer with materials and boundary conditions labeled. The stainless steel soldering iron is connected to a transducer consisting of the PZT sandwiched between two aluminum end caps.

Table 1
Material properties used in the simulations.

Material	Bulk modulus [GPa]	Poisson's ratio	Density [kg/m^3]	Viscosity [Pa s]
Aluminum	69.6	0.33	2770	N/A
Stainless Steel	169	0.31	7750	N/A
PZT	31	0.17	7500	N/A
BiSn Solder	41	0.30	8500	0.00135

$$[(1 - i\gamma\omega)\boldsymbol{K_s} - \omega^2\boldsymbol{M_s}]\boldsymbol{u_s} = \boldsymbol{F_s} \tag{1}$$

where $\boldsymbol{K_s}$ and $\boldsymbol{M_s}$ are global stiffness and mass matrices. Material damping is incorporated using a small constant damping ratio of $\xi = 0.01$ with loss factor $\gamma = 2\xi = 0.02$, which models the effects of viscous damping in metals operating in their elastic ranges.

2.1. Natural frequencies

Since the thin support ring provides only very small added stiffness and mass, the natural frequencies computed from the model with free boundary conditions match closely with those including the ring support. For the Type A and Type B assemblies, we neglect the small structural damping and compute the natural frequencies from the mass and stiffness properties. The natural frequencies ω_j and corresponding mode shapes $\boldsymbol{\varphi_j}$ are extracted by solving the generalized eigenvalue problem,

$$[\boldsymbol{K_s} - \omega_j^2\boldsymbol{M_s}]\boldsymbol{\varphi_j} = \boldsymbol{0}. \tag{2}$$

Modes are decomposed into axial, torsional and bending types. For reference, typical axial and bending mode shapes for the Type A assembly are shown in Fig. 3. Since the transducer applies an axial force to the assembly, we filter the axial modes from the other types of modes shapes.

For proprietary reasons, modal frequencies f are normalized by the relationship,

$$f_{\text{norm}} = \frac{f - f_1}{f_2 - f_1}, \tag{3}$$

where f_2 and f_1 are the upper and lower limits of the frequency range of interest. Hereafter, frequency will refer to the normalized frequency f_{norm}. Due to this normalization, frequencies that exist above and below the frequency range are not included in the filtered results. The normalized natural frequencies within the range of interest are shown in Table 2 for the complete assembly. For reference, the normalized optimal target resonance frequency is $f_{\text{norm}} = 0.4$, with an assumed operating range of the driver as $f_{\text{norm}} = 0.4 \pm 0.03$. This frequency corresponds to the maximal power delivered from the control unit.

There are three modes for the Type A Iron Assembly within the range of interest, while there is just one mode for the Type B Iron Assembly. Both Type A and Type B irons use the same piezoelectric transducer composed of the PZT and aluminum end pieces. The difference between the Type A and Type B irons are the segment lengths and sectional properties. Both the Type A and Type B component stack assemblies with transducer have resonance frequencies tuned to match closely with the 0.4 target and lie within the operating range of the control unit driver for optimal displacement amplitude and power. For the Type A assembly, the frequency is 0.03 below the optimal 0.4 target, while the Type B assembly is 0.02 above the optimal target frequency.

2.2. Frequency-response

In order to quantify how the two different soldering irons respond to a change in operating frequency, a frequency-response analysis was performed for the complete assembly of soldering iron with transducer. To increase stability, we use the small damping factor $\gamma = 2\xi$ previously discussed. In each case, the loading condition shown in Fig. 2 was applied and the magnitude of the tip displacement (u) was calculated. We apply a unit force to the transducer to drive the solder stack assembly, because the exact form of the mechanical displacement response from the PZT material is not known. The tip displacement magnitude u is normalized with the input driving force F and the relative amplitude response with frequency is quantified.

The frequency-response of the Type A and B solder iron assemblies are shown in Fig. 4. The amplitude resonance peaks occur at the damped natural frequencies, which match closely with the undamped natural frequencies presented in Table 2. The Type B assembly has higher peak displacement amplitude and a larger bandwidth near the target resonance of 0.4, making it less susceptible to power loss from small changes in input frequencies. In both cases, the resonance frequencies are within the assumed operating range of the driver. The larger bandwidth provides a more robust design that can still provide a large tip displacement amplitude even without perfect tuning. Further tuning of the system to shift frequency to a precise target can be achieved by changing the dimensions of soldering irons and/or the

Fig. 3. Typical (*a*) axial and (*b*) bending mode shapes for the Type A soldering tip.

Table 2
Normalized natural frequencies, f_{norm}, corresponding to axial modes of the two iron assemblies. Target operating normalized frequency is 0.4 ± 0.03.

Type A	Type B
0.10	
0.37	0.42
0.91	

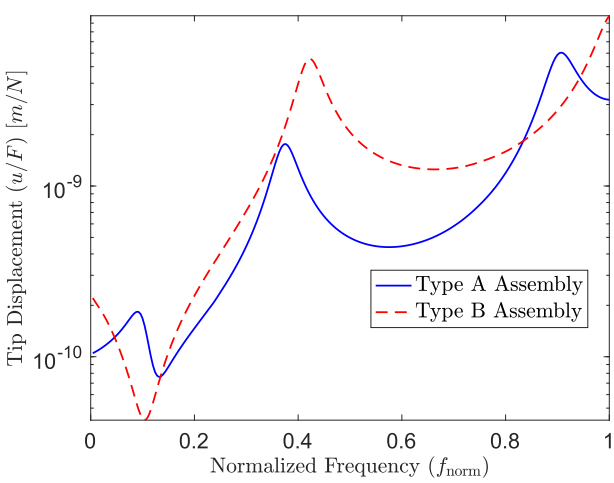

Fig. 4. Frequency response for Type A and Type B solder iron assemblies plotting the normalized tip displacement u/F ([displacement]/[unit applied force]) against applied frequency f_{norm}. The normalized target operating frequency for the transducer is 0.4 ± 0.03.

aluminum end caps of the transducer, altering the added mass and stiffness properties.

2.3. 1D model

To facilitate rapid design optimization of length, cross-section, and material properties, a simplified one-dimensional (1D) model of the solder iron stack assembly has been developed. The 1D model has simplified geometry with notches and fillets removed, as shown in Fig. 5.

We begin by providing a brief description of the 1D model, which has the ability to implement different material properties through the cross-section and tapering along the axial dimension. For example, this is seen in the steel thread mated with the aluminum end pieces of the transducer shown in Figs. 2 and 5. Using the principle of virtual work, the variational form for the one-dimensional model problem can be stated as: given a driving frequency ω and applied force amplitude F at location x_L, find the axial displacement $u(x)$, for all variations (virtual displacements) $w(x)$ such that the variational equation (weak form) is satisfied,

$$\int_0^L E'\frac{dw}{dx}\frac{du}{dx}\,dx + k_0 w(x_0)u(x_0) - \omega^2\int_0^L \rho' w\,u\,dx = w(x_F)F \tag{4}$$

where,

$$E' = \sum_{l=1}^{n} E_l A_l, \qquad \rho' = \sum_{l=1}^{n} \rho_l A_l \tag{5}$$

and k_0 is a discrete axial spring located at x_0 corresponding to the circular flange support. Here, E_l is the elastic moduli and ρ_l the mass density of the different materials within the composite, while E' is the effective axial modulus for a composite cross-section and ρ' is the effective mass per unit length. The total cross-section area is the sum of individual composite areas $A = \sum A_l$.

The discrete spring $k_0 = (Et^3)/(ca^2)$ is a simplified model of the axial stiffness of the circular flange support obtained from an analytical solution for the center deflection of a thin, flat circular annulus of thickness t, with outer edge fixed [26]. Here c is a factor that depends upon the ratio a/b, where a and b are the outer and inner radius of the thin annulus, respectively.

While an analytical solution or an assumed modes solution to this problem is feasible based on (4), for convenience and ease of automating changes in material property distribution and geometry, a finite element solution is developed. Using the linear approximation for displacement $u(x)$ within each 2-node composite bar element with uniform cross-section area along the axial dimension (with capability of variable materials within the cross-section), the element stiffness and mass matrices resulting from the discrete form of the variational Eq. (4) can be expressed as,

$$\boldsymbol{k}_e e = \frac{E'_e}{\ell_e}\begin{bmatrix} 1 & -1 \\ -1 & 1 \end{bmatrix}, \qquad \boldsymbol{m}_e = \frac{\rho'_e \ell_e}{6}\begin{bmatrix} 2 & 1 \\ 1 & 2 \end{bmatrix} \tag{6}$$

where ℓ_e is the element length, and E'_e and ρ'_e are the effective axial modulus and mass per unit length of the composite section.

In the case of tapered bar segments with uniform material properties and circular cross-section $A(x) = \pi r^2(x)$, with linearly varying radius $r(x)$,

Fig. 5. Visualization of the simplified geometry used in the 1D model of the Type A soldering iron assembly.

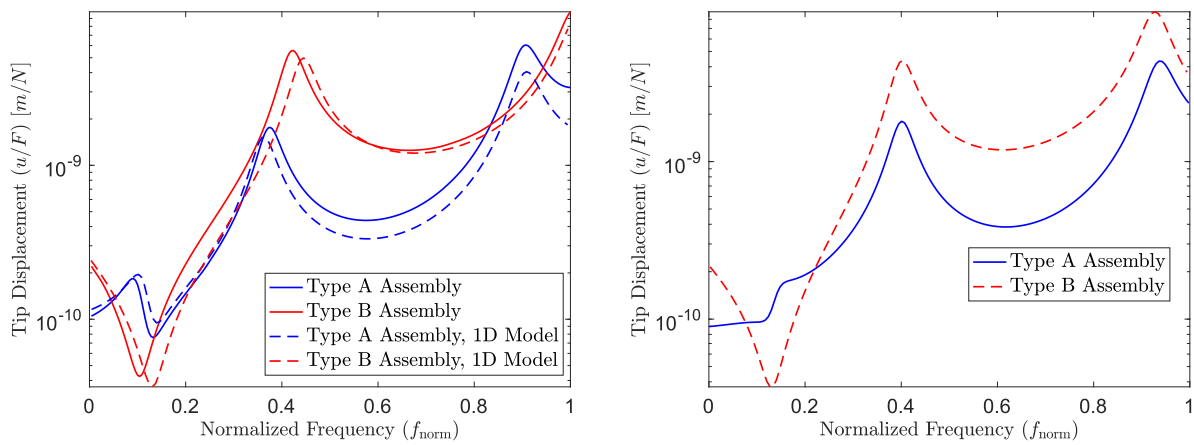

(a) Comparison between 1D and 3D models (b) Optimized

Fig. 6. Frequency response plotting normalized displacement u/F against applied frequency f_{norm} for Type A and Type B assemblies showing (*a*) the comparison between the 1D and 3D models of the soldering iron assemblies and (*b*) the optimized geometries for a normalized target frequency $f_{\text{norm}} = 0.4$.

$$\boldsymbol{k}_e = \frac{\pi(r_1^2 + r_1 r_2 + r_2^2)E_e}{3\ell_e}\begin{bmatrix} 1 & -1 \\ -1 & 1 \end{bmatrix}, \tag{7}$$

$$\boldsymbol{m}_e = \frac{\rho_e \ell_e \pi}{60}\begin{bmatrix} 2(6r_1^2 + 3r_1 r_2 + r_2^2) & (3r_1^2 + 4r_1 r_2 + 3r_2^2) \\ (3r_1^2 + 4r_1 r_2 + 3r_2^2) & 2(r_1^2 + 3r_1 r_2 + 6r_2^2) \end{bmatrix} \tag{8}$$

where r_1 and r_2 are the circular radius at the end nodes of the element. After element assembly, the global finite element equations take the form of (1). The discrete spring k_0 is added to the diagonal of the matrix equations in row/column number corresponding to the node number placed at the circular flange support x_0.

The 1D finite element model is readily coded in Matlab, where segment geometric dimensions are easily changed to optimize the resonance frequency of the solder iron stack. We use preliminary results from the 1D model design tool to demonstrate that further optimization of the geometry of the 3D finite element model can be made. For the 1D model, converged results are obtained using between 16 and 40 elements within the different geometric segments for a total of 210 elements. For the 3D model, converged results are obtained using ANSYS with quadratic tetrahedral elements with a body size mesh of 1 mm which captured the small geometric features of the solder iron stack. Fig. 6(*a*) shows close agreement in the frequency response between the 1D and 3D finite element models. To demonstrate the utility of the 1D model, Fig. 6(*b*) shows optimized results that match the normalized frequency target for optimal power obtained by changing the length of the iron segment below the circular ring flange support by less than 15 percent. Results show that the tip displacement of the Type B assembly is nearly 4 times greater than that of the Type A assembly. This implies the Type B assembly is able to more efficiently deliver acoustic power to the tip and ultimately the molten solder pool.

3. Solid-fluid interaction

A coupled solid-fluid model is created to model acoustic pressure in the molten solder, which provides a means to understand how the acoustical design of the Type A and B assemblies affect pressure variations in the solder. A higher pressure in the solder is one of the key factors to drive cavitation and it is hypothesized this high localized pressure yields better surface cleaning, and thus improved adhesion of the solder to the substrate surface [24]. Our goal in these simulations is to examine the trend in maximum acoustic pressure in the solder as a function of tip height above the substrate, which we treat as our process parameter.

We utilize the Acoustics application within ANSYS for this analysis [27]. The application solves a linearized version of the Navier-Stokes equations for the fluid resulting in a wave equation for acoustic pressure the includes dissipative effects from fluid viscosity. The fluid is modeled as compressible with small pressure changes with respect to the mean pressure, and is non-flowing. For the time-harmonic response, the reduced wave equation in the fluid domain Ω_f is [27]:

$$\left(\frac{1}{\rho_0} + i\omega\frac{4\mu}{3\rho_0^2 c^2}\right)\nabla^2 p + \omega^2\frac{1}{\rho_0 c^2}p = 0. \tag{9}$$

The corresponding weak integral form over the fluid domain Ω_f is,

$$\int_{\Omega_f}\left\{\left(\frac{1}{\rho_0} + i\omega\frac{4\mu}{3\rho_0^2 c^2}\right)\nabla w_f \cdot \nabla p - \omega^2\frac{1}{\rho_0 c^2}w_f p\right\}dV + \omega^2\int_{\Gamma_f} w_f\,\boldsymbol{u}\cdot\boldsymbol{n}\,ds = 0, \tag{10}$$

where $c = \sqrt{K/\rho_o}$ is the speed of sound in the fluid medium, ρ_o is the mean fluid density, K is the bulk modulus of the fluid, μ is the viscosity, and p is the acoustic pressure, $\boldsymbol{u}$ is the displacement vector, w_f is a test function, and $\boldsymbol{n}$ is the outward normal unit vector to the fluid boundary Γ_f.

The coupled structural-acoustic model was set up with the soldering iron tip immersed in the liquid solder pool modeled by a rectangular prism fluid domain with 1.5 mm depth, 2.0 mm width and length 12.5 mm. The tip height h is related to the solder height a and depth of solid/fluid interface b by $h = a - b$, as shown in Fig. 7. These dimensions represent a typical experimentally-observed solder bead on a flat substrate in our ultrasonic-assisted soldering platform. Unstructured tetrahedral finite element meshing was used for discretization of the geometry. A mesh size study was performed to evaluate the model convergence when driven at the operating frequency ensuring accurate results were obtained. For the acoustic fluid region modeling the solder pool, this resulted in a body sized tetrahedral element mesh size of 0.3 mm applied to the solder pool with spherical mesh refinement at the tip-fluid interface area, where a 1.5 mm radius spherical volume was enhanced to 0.01 mm resolution for convergence. The solder tip and stack was meshed with tetrahedral elements with a body size mesh of 1 mm. This meshing process produced an efficient mesh distribution with a fine grid near the solid-fluid interface capturing changing pressure gradients. The boundary conditions applied to the solder pool are shown in Fig. 7; the free surfaces of the solder pool are modeled with idealized pressure-release $p = 0$ boundary conditions [28], the solder/substrate interface is modeled as a rigid boundary with vanishing derivative of pressure normal to the boundary $\frac{\partial p}{\partial n} = \nabla p \cdot \boldsymbol{n} = 0$ (Neumann conditions), the absorptive boundary condition in the far-field models waves passing through this truncated boundary [27,29]. The interface between the solder tip (solid) and solder melt (fluid) couples the solid

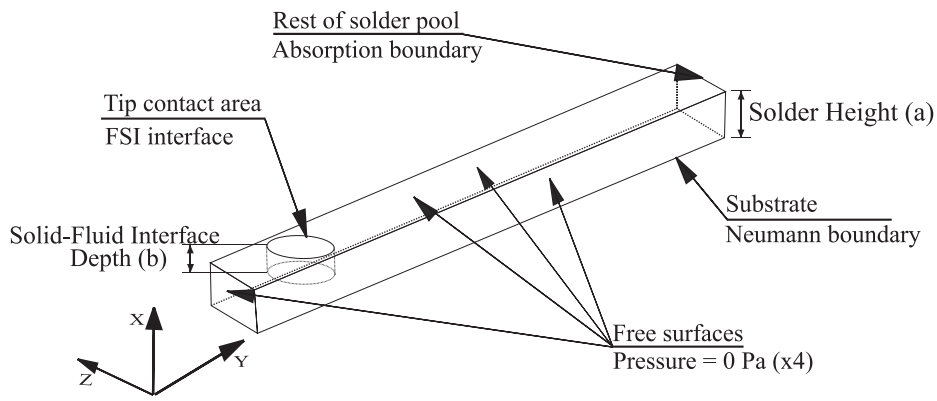

Fig. 7. Schematic diagram of the boundary conditions for the solid-fluid interaction model. The tip height $h = a - b$, above the substrate, is defined by the difference in the solder height a and the depth b of the cylindrical solid-fluid interface for the tip.

and fluid domains and have fluid-structure interaction (FSI) pressure and displacement conditions applied there. Boundary conditions not shown in Fig. 7 include the fixed support on the iron mount and the driving force at the piezoelectric transducer (cf. Fig. 2). The symmetric form of the coupled solid-fluid finite element equations are [28,27],

$$(\boldsymbol{K}_s - \omega^2\boldsymbol{M}_s + i\omega\boldsymbol{C}_s)\boldsymbol{u}_s - i\omega\boldsymbol{R}\boldsymbol{q}_f = \boldsymbol{F}_s$$
$$-(\boldsymbol{K}_f - \omega^2\boldsymbol{M}_f + i\omega\boldsymbol{C}_f)\boldsymbol{q}_f - i\omega\boldsymbol{R}^T\boldsymbol{u}_s = \frac{i}{\omega}\boldsymbol{F}_f$$

where $\boldsymbol{p}_f = i\omega\boldsymbol{q}_f$ are nodal acoustic pressures, $\boldsymbol{u}_s$ the nodal displacements for the structure, and $\boldsymbol{R}$ a fluid-structure coupling matrix.

The material properties used in the simulations are listed in Table 1. Type A and Type B assemblies use the same materials properties described in the solid acoustic analysis in Section 2. The bismuth based solder is composed, in percent of weight, of 52% Bismuth, 48% tin, and 0.18% titanium. The solder bulk modulus property and solder viscosity has been reported by Kamioka [30], and Lee et al. [31].

3.1. Results

The transducer applies a sinusoidal driving force with normalized operating frequency $f_{\text{norm}} = 0.4$ and unit amplitude. The resulting acoustic field is transmitted through the solder iron assembly and generates an acoustic pressure in the liquid solder pool, as shown in Figs. 8 and 9. Fig. 8 shows the spatial distribution of pressure for the Type A assembly which illustrates the tip focuses the acoustic energy toward the centerline of the tip resulting in maximum pressure. A similar pressure distribution was found for the Type B iron assembly, but with different amplitudes.

Our interest is in analyzing how the pressure varies with the tip height h above the substrate, which we vary between 0.1 mm and 1 mm in our analysis. The results for $h = 0.1$ mm and $h = 0.5$ mm are shown in Fig. 9(a) and (b), respectively. In both cases, the maximum pressure occurs at the solid-liquid interface located at the bottom of the solder tip and can be seen to focus towards the centerline of the tip. Fig. 9(c) shows the maximum acoustic pressure rapidly decreases with increasing tip height. The acoustic pressure generated from the Type B assembly is significantly greater than that of the Type A assembly, which we attribute to the relative magnitude of the tip displacement seen in the frequency response of the solid acoustics (cf. Fig. 4(b)). This implies the Type B assembly is able to more efficiently deliver acoustic power from the tip into the molten solder pool.

4. Experiment

Acoustic pressure drives the nucleation and collapse of bubbles in the molten solder pool that is responsible for the enhanced adhesive bond at the solder/substrate interface. Our model shows that the acoustic pressure strongly depends upon the tip height (cf. Fig. 9(c)). We are interested in experimentally verifying this prediction and quantifying the strength of the adhesive bond as it depends upon this process parameter. We use optical microscopy to determine the fractional contact area of the bond at the solder/substrate interface, which we will use as a proxy for adhesion.

A series of experiments are conducted with our automated ultrasonic soldering unit described above using the Type B solder tip assembly. Three test specimens (Slides 0002, 0003, 0004) were created using identical experimental conditions (tip speed, solder feed rate, ultrasonic power, substrate and tip temperatures). Each specimen consisted of 10 solder lines with the tip height ranging from 0.05 mm to 1.00 mm. Each solder line was imaged at five different locations along its length using a microscope. This resulted in 150 micrographs. A sample image is shown in Fig. 10(left). Here voids appear black, while the solder/substrate contact area appears grey. The typical void size is about 5–8 μm for the large-sized, 1–2 μm for the medium-sized, and about 0.5 μm for the smallest voids visible. The fractional contact area, or contact area normalized by total area, is computed using image processing algorithms in MATLAB. The program filters the raw image and creates a binary image (cf. Fig. 10(right)) from which the fractional contact area can be computed [32].

Fig. 8. Contour map showing the spatial dependence of the normalized pressure for the Type A assembly, measured in units of Pa/N, on the substrate surface $z = 0$ at a tip height $h = 0.1$ mm.

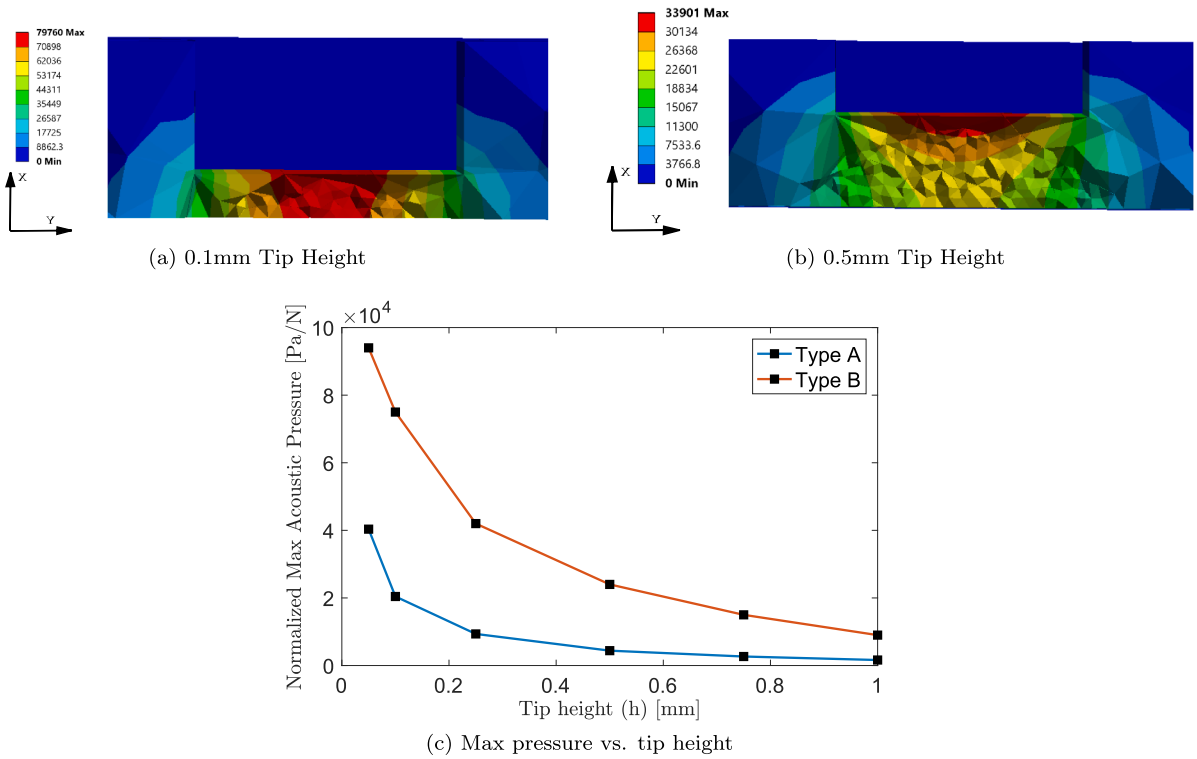

(a) 0.1mm Tip Height

(b) 0.5mm Tip Height

(c) Max pressure vs. tip height

Fig. 9. (*a*, *b*) Spatial dependence of the normalized pressure for Type B assembly, measured in units of Pa/N, in a vertical cross section through the center of the solder tip for tip heights (*a*) $h = 0.1$ mm and (*b*) $h = 0.5$ mm. (*c*) The maximum normalized acoustic pressure in the solder pool is plotted against the tip height h and is shown to decrease with increasing tip height contrasting Type A and Type B assemblies.

Fig. 11(*a*) plots the measured contact area against the tip height for all 150 micrographs. It is important to note the variation in measured contact area for a fixed tip height both (i) within a given solder line (fixed Slide #) as well as (ii) between sample slides. Such variation could be related to the manufacturing process, the physics of solidification, the image processing algorithm, or some combination of those aforementioned factors. However, one should note the range of the data is relatively tight considering the number of factors that influence the ultrasonic soldering process. Despite these variations, there is a distinct observable trend where the contact area decreases for increasing tip height. This becomes even more clear through a statistical analysis of the raw data. Fig. 11(*b*) plots the average contact area with standard 95% confidence intervals. Note the relatively small confidence intervals. Of note is the outlier at a tip height of 0.4 mm that shows both the tightest grouping and highest contact area, which we attribute to any number of effects such as non-uniform heat transfer, phase change, or hydrodynamics due to the presence of a wake from the moving tip. Nonetheless, there is a clear decreasing trend, consistent with the decrease in maximum gauge pressure with increasing tip height shown in Fig. 9(*c*). Multiple fitting functions were tried for Fig. 9(*c*) and the exponential gave the best fit. To test the hypothesis that porosity was linked to the maximum pressure the same exponential functional form was used to fit the curve of contact area versus tip height in Fig. 11(*b*) (solid line). Although the R^2 value of the fit is low, it confirms the general decreasing trend that is consistent with our understanding of the relationship between the acoustic pressure in the solder melt and the adhesive bond between the solder and substrate. With regard to process optimization, it is clear the best solder quality was achieved by placing the tip as close to the substrate as possible.

5. Conclusion

In this paper, we use finite-element analysis to describe the acoustics in the ultrasonic soldering process from the PZT transducer through the soldering iron tip and into the molten solder pool. A one-dimensional finite element model was developed as a design tool to quickly optimize the geometry and material properties of the solder stack assembly in order to to properly tune the system to the transducer frequency, which results in tip displacement of the Type B assembly that is nearly 4 times greater than that of the Type A assembly. The full solid-

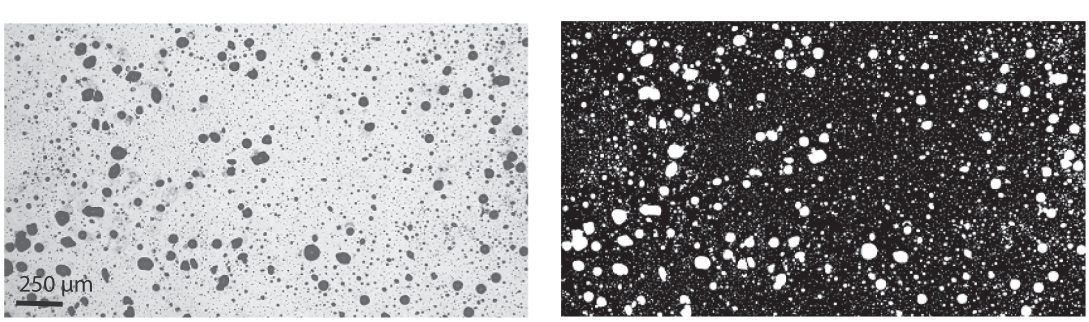

Fig. 10. Microscopy image (left) of the underside of the glass slide showing the solder/substrate interface of a typical solder line. Image processing results in a binary image (right) where voids are represented as white areas and solid contact as black areas.

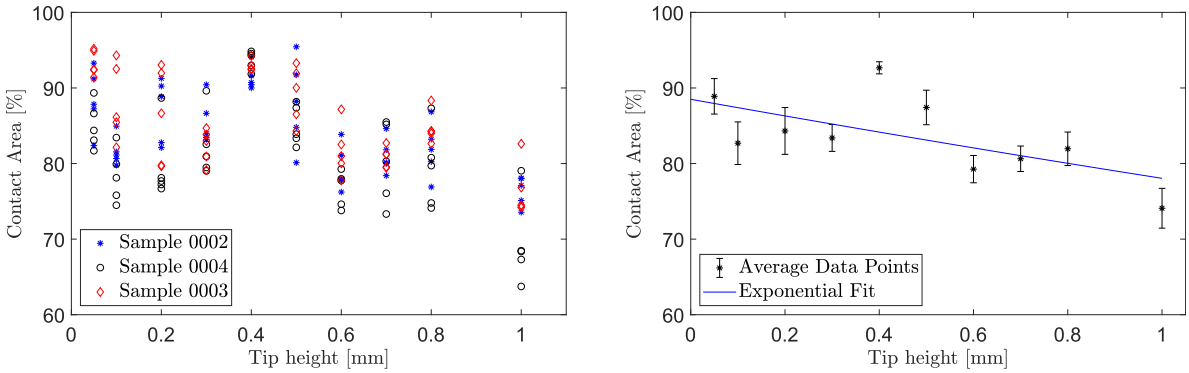

(a) All data points (b) Average values and Curve Fit

Fig. 11. (*a*) Contact area measured at five locations along the length of the solder line against tip height *h*. The three samples were run using identical experimental conditions and demonstrates the variability in the US soldering process. (*b*) The average value of contact area shows a decreasing trend with increasing tip height. The solid line is the best fit of the data to an exponential curve. Error bars are 95% confidence intervals.

fluid interaction simulation (from transducer to solder pool) gives the acoustic pressure distribution in the liquid solder melt and we use the maximum value as a measure of cavitation and ultimately the adhesive bond strength at the solder/substrate interface. Our results compare favorably to preliminary experiments which show the increasing tip height (process parameter) decreases the maximum pressure in the solder pool with a commensurate decrease in porosity at the solder joint, a measure of adhesion.

The models we have developed provide a useful design tool for improving the ultrasonic soldering process, as well as understanding the mechanisms that lead to improved adhesion. Further refinement of the models are planned to include attenuation effects due to the interaction of cavitation bubbles in the molten solder [33], surface tension effects at the liquid/gas interface [34,35], and phase-change (solidification) during cooling [36]. Further experimental testing is planned to measure bond strength from a mechanical shear test.

Acknowledgements

We would like to acknowledge the Harris Corporation and the Clemson University Calhoun Honor's College for supporting this research effort. We would also like to thank Hyrel 3D for their technical assistance.

References

[1] J.N. Antonevich, Fundamentals of ultrasonic soldering, Weld. J. 55 (July 1976) 200–207.
[2] Hamid R. Faridi, A new look at flux-free ultrasonic soldering, Weld. J. 79 (9) (2000) 41–45.
[3] V.L. Lanin, Ultrasonic soldering in electronics, Ultrason. Sonochem. 8 (4) (2001) 379–385.
[4] S.K. Kang, W.K. Choi, M.J. Yim, D.Y. Shih, Studies of the mechanical and electrical properties of lead-free solder joints, J. Electron. Mater. 31 (11) (2002) 1292–1303.
[5] Hongjun Ji, Qiang Wang, Mingyu Li, Microstructural evolution of lead-free solder joints in ultrasonic-assisted soldering, J. Electron. Mater. 45 (1) (2016) 88–97.
[6] Daisuke Yonekura, Tomoyuki Ueki, Kazushige Tokiyasu, Shuji Kira, Toshio Wakabayashi, Bonding mechanism of lead-free solder and glass plate by ultrasonic assisted soldering method, Mater. Des. 1980–2015 (65) (2015) 907–913.
[7] Japan Unix, Fundamental soldering technologies vol 3: Ultrasonic wave edition, 2013. www.japanunix.com.
[8] Zhiwu Xu, Zhengwei Li, Yushi Qi, Jiuchun Yan, Soldering porous ceramics through ultrasonic-induced capillary action and cavitation, Ceram. Int. (2019).
[9] Hamid Reza Faridi, Flux-free ultrasonic soldering of aluminum and stainless steel, Scholar Arch. (3328) (2000).
[10] Zhengwei Li, Xu. Zhiwu, Lin Ma, Sheng Wang, Xuesong Liu, Jiuchun Yan, Cavitation at filler metal/substrate interface during ultrasonic-assisted soldering. Part i: Cavitation characteristics, Ultrason. Sonochem. 49 (2018) 249–259.
[11] Zhengwei Li, Zhiwu Xu, Lin Ma, Sheng Wang, Xuesong Liu, Jiuchun Yan, Cavitation at filler metal/substrate interface during ultrasonic-assisted soldering. Part ii: Cavitation erosion effect, Ultrason. Sonochem. 50 (2019) 278–288.
[12] Lord Rayleigh, Viii. On the pressure developed in a liquid during the collapse of a spherical cavity, The London, Edinburgh, Dublin Philosoph. Mag. J. Sci. 34 (200) (1917) 94–98.
[13] Milton S. Plesset, The dynamics of cavitation bubbles, J. Appl. Mech. 16 (1949) 277–282.
[14] Christopher E. Brennen, Cavitation and Bubble Dynamics, Cambridge University Press, 2013.
[15] Milton S. Plesset, Andrea Prosperetti, Bubble dynamics and cavitation, Annu. Rev. Fluid Mech. 9 (1) (1977) 145–185.
[16] Vladimir S. Ajaev, G.M. Homsy, Modeling shapes and dynamics of confined bubbles, Annu. Rev. Fluid Mech. 38 (2006) 277–307.
[17] Andrea Prosperetti, Vapor bubbles, Annu. Rev. Fluid Mech. 49 (2017).
[18] Benjamin Dollet, Philippe Marmottant, Valeria Garbin, Bubble dynamics in soft and biological matter, Annu. Rev. Fluid Mech. 51 (1) (2019) 331–355.
[19] Timothy Leighton, The Acoustic Bubble, Academic Press, 2012.
[20] Milton S. Plesset, Richard B. Chapman, Collapse of an initially spherical vapour cavity in the neighbourhood of a solid boundary, J. Fluid Mech. 47 (2) (1971) 283–290.
[21] Yong Xiao, Qiwei Wang, Ling Wang, Xian Zeng, Mingyu Li, Ziqi Wang, Xingyi Zhang, Xiaomeng Zhu, Ultrasonic soldering of Cu alloy using Ni-foam/Sn composite interlayer, Ultrason. Sonochem. 45 (2018) 223–230.
[22] B. Eo Noltingk, Eo A. Neppiras, Cavitation produced by ultrasonics, Proc. Phys. Soc. London, Sect. B 63 (9) (1950) 674.
[23] Kyuichi Yasui, Acoustic Cavitation and Bubble Dynamics. Spring Briefs in Molecular Science, Ultrasound and Sonochemistry, Springer, 2018.
[24] Alexander A. Doinikov, Benjamin Dollet, Philippe Marmottant, Model for the growth and the oscillation of a cavitation bubble in a spherical liquid-filled cavity enclosed in an elastic medium, Phys. Rev. E 97 (2018) 013108.
[25] MEMSnet, Material: Lead zirconate titanate (PZT), 2018.
[26] A.P. Boresi, R.J. Schmidt, Advanced Mechanics of Materials, sixth ed., John Wiley & Sons, 2003.
[27] Ansys, Inc. ANSYS Mechanical APDL Theory Reference, release 15.0 edition, 2013.
[28] G.C. Everstine, Finite element formulations of structural acoustics problems, Comput. Struct. 65 (3) (1997) 307–321.
[29] Lonny Thompson, Peter Pinsky, Acoustics, in: Erwin Stein, Rene de Borst, Thomas J.R. Hughes (Eds.), Encyclopedia of Computational Mechanics, vol. 4, second ed., John Wiley & Sons, 2017.
[30] Hiroaki Kamioka, Temperature variations of elastic moduli up to eutectic temperature in tin-bismuth alloys, Jpn. J. Appl. Phys. 22 (12) (1983) 1805–1809.
[31] Jong Ho Lee, Dong Nyung Lee, Use of thermodynamic data to calculate surface tension and viscosity of Sn-based soldering alloy systems, J. Electron. Mater. 30 (9) (2001).
[32] Mathworks, Detecting a cell using image segmentation, 2019.
[33] Fushi Bai, Yangyang Long, Kai-Alexander Saalbach, Jens Twiefel, Theoretical and experimental investigations of ultrasonic sound fields in thin bubbly liquid layers for ultrasonic cavitation peening, Ultrasonics 93 (2019) 130–138.
[34] S.H. Davis, Thermocapillary instabilities, Annu. Rev. Fluid Mech. 19 (1987) 403–435.
[35] J.B. Bostwick, Spreading and bistability of droplets on differentially heated substrates, J. Fluid Mech. 725 (2013) 566–587.
[36] S.H. Davis, Cambridge Monographs on Mechanics. Theory of Solidification, Cambridge University Press, 2001.